Comparison of Fully-Compressible Equation Sets for Atmospheric Dynamics

Nash'at N. Ahmad*
NASA Langley Research Center, Hampton, Virginia, 23681

Traditionally, the equation for the conservation of energy used in atmospheric models is based on potential temperature and is used in place of the total energy conservation. This paper compares the application of the two equations sets for both the Euler and the Navier-Stokes solutions using several benchmark test cases. A high-resolution wave-propagation method which accurately takes into account the source term due to gravity is used for computing the nonhydrostatic atmospheric flows. It is demonstrated that there is little to no difference between the results obtained using the two different equation sets for Euler as well as Navier-Stokes solutions.

I. Introduction

Von Helmholtz introduced the concept of potential temperature in 1888 and termed it *waermegehalt* (Bauer 1908), which translates into "heat(warmth) content". According to von Helmholtz's definition, *waermegehalt* was the heat of an air mass measured in terms of absolute temperature, if that air mass were to be brought to reference temperature and pressure by an adiabatic process. Von Bezold suggested that the proposed quantity should be named potential temperature which was more descriptive and accurate (Bauer 1908). Traditionally, the atmospheric flow models have replaced the conservation of total energy equation in the Euler and Navier-Stokes equations with the conservation of potential temperature. An early use of this equation set can be found, for example, in Lilly (1962). The early operational meso- and micro-scale models such as the Regional Atmospheric Modeling System (RAMS) developed by Pielke et al. (1993), Mesoscale Model 5 (MM5) developed by Dudhia et al. (1993), the Naval Research Laboratory's Coupled Ocean/Atmosphere Mesoscale Prediction System (COAMPS) by Hodur (1997), and the Advanced Regional Prediction System (ARPS) by Xue et al. (2000) used potential temperature in the energy conservation equation. The current operational models also use potential temperature conservation instead of total energy conservation. These include the Operational Multiscale Environment model with Grid Adaptivity (OMEGA) model (Bacon et al. 2000), the Weather Research and Forecast (WRF) model developed at the National Center for Atmospheric Research by Klemp et al. (2000), and the Consortium for Small Scale Modeling (COSMO) model (Baldauf et al. 2011).

The conservation of total energy equation has rarely been used for atmospheric flow simulations. Some exceptions are, Klassen et al. (2003) who have studied gravity wave formation over mountains, and the simulations of wave generation in the mesosphere by Snively and Pasko (2003). While comparisons between different flow models that use potential temperature as conservation of energy have been conducted in the past (e.g., Straka et al. 1993), the number of studies that compare the compressible equation set (conservation of energy in terms of total energy) with the approximation used in atmospheric modeling (potential temperature conservation) have been limited. Ahmad et al. (2007) compared the two equation sets (viscous terms were not included and only Euler solutions were considered) and found the results from the two models to be comparable. The numerical techniques used in that study however, were different for the two equation sets. Giraldo and Restelli (2008) conducted a comprehensive study in which they compared three different formulations for both the Euler and the Navier-Stokes equations. They found that the results of the two different forms of compressible equations sets (conservation of total energy *vs.* conservation of potential temperature) were almost identical. Giraldo and Restelli (2008) pointed out that the true viscous stresses are accounted for when using the conservation of total energy equation. Ahmad (2009) conducted a quantitative analysis of mass and energy conservation properties of the two models and found little to no difference between the two (only Euler solutions were considered). In the current study, the two equation sets are further evaluated and compared using different benchmark test cases. Giraldo and Restelli (2008) used the perturbation form of equations in their study,

* Research Aerospace Engineer, NASA, Hampton, Virginia. Senior Member, AIAA.

whereas this study computes the equations in their original form. This study is also extended to include Navier-Stokes solutions. In the following sections, the governing equations, the numerical technique, and the results of several benchmark tests are described in detail. Throughout, the terms potential temperature and theta equation are used interchangeably.

II. Governing Equations

The basic equations governing fluid flow comprise a set of partial differential equations for the conservation of mass, momentum, and energy. An equation of state is needed to close the system:

$$\frac{\partial \mathbf{U}}{\partial t}+\frac{\partial \mathbf{F}}{\partial x}+\frac{\partial \mathbf{G}}{\partial z}=\frac{\partial \mathbf{F_v}}{\partial x}+\frac{\partial \mathbf{G_v}}{\partial z}+\psi+S\,, \tag{1}$$

where **U** is vector of conserved variables, **F** and **G** are the flux vectors, and ψ is the source term due to gravity. $\mathbf{F_v}$ and $\mathbf{G_v}$ are the viscous flux vectors. S represents the heat sinks and sources due to microphysical processes and atmospheric radiative transfer. In this study the atmosphere is assumed to be dry and therefore the source term S in Eq. (1) is set to zero. If the viscous dissipation terms are neglected, Eq. (1) simplifies to the Euler equations:

$$\frac{\partial \mathbf{U}}{\partial t}+\frac{\partial \mathbf{F}}{\partial x}+\frac{\partial \mathbf{G}}{\partial z}=\psi\,, \tag{2}$$

where

$$\mathbf{U}=\begin{bmatrix}\rho\\ \rho u\\ \rho w\\ E\end{bmatrix},\qquad \mathbf{F}=\begin{bmatrix}\rho u\\ \rho u^2+p\\ \rho uw\\ u(E+p)\end{bmatrix},\qquad \mathbf{G}=\begin{bmatrix}\rho w\\ \rho uw\\ \rho w^2+p\\ w(E+p)\end{bmatrix},\qquad \psi=\begin{bmatrix}0\\ 0\\ \rho g\\ \rho wg\end{bmatrix}. \tag{3}$$

In Eq. (3), ρ is the density of fluid, u is the velocity component in the x-direction, w is the velocity component in the z-direction and p is the pressure. E is the total energy per unit volume:

$$E=\rho\frac{1}{2}(u^2+w^2)+\rho e\,, \tag{4}$$

where $\frac{1}{2}(u^2+w^2)$ is the specific kinetic energy and e is the specific internal energy given by an equation of state. For an ideal gas:

$$e=\frac{p}{(\gamma-1)\rho}\,. \tag{5}$$

In the above relations, γ is the ratio of specific heats and g is the acceleration due to gravity acting in the vertical (z-axis) direction. Eq. (3)-(5) are rarely used for atmospheric flow computations. Some exceptions include, Klassen et al. (2003), Snively and Pasko (2003), Ahmad et al. (2007), and Giraldo and Restelli (2008).

For atmospheric flows the equation for conservation of total energy in Eq. (2)-(5) is replaced by the conservation of potential temperature:

$$\mathbf{U}=\begin{bmatrix}\rho\\ \rho u\\ \rho w\\ \rho\theta\end{bmatrix},\qquad \mathbf{F}=\begin{bmatrix}\rho u\\ \rho u^2+p\\ \rho uw\\ u\rho\theta\end{bmatrix},\qquad \mathbf{G}=\begin{bmatrix}\rho w\\ \rho uw\\ \rho w^2+p\\ w\rho\theta\end{bmatrix},\qquad \psi=\begin{bmatrix}0\\ 0\\ \rho g\\ 0\end{bmatrix}, \tag{6}$$

where θ is the potential temperature. The system is closed by an equation of state for pressure,

$$p = C_0 (\rho\theta)^{\gamma} . \tag{7}$$

C_0 in Eq. (7) is a constant given by:

$$C_0 = \frac{R_d^{\gamma}}{p_0^{R_d / C_v}} . \tag{8}$$

In the above relations, R_d is the gas constant for dry air. C_p and C_v are the specific heats of air at constant pressure and volume respectively. p_0 is the reference base-state pressure. The conservation laws given in Eq. (6)-(8) are hyperbolic (Ahmad et al. 2005; Ahmad and Lindeman 2007). The primitive variable transformation of Eq. (6)-(8) was derived and found to be identical to the transformation for the total energy conservation equations (Appendix A). This result implies that for smooth solutions, the two models should give identical results.

The viscous terms, however are treated differently in the two models. In the total energy equation set, the viscous fluxes, $\mathbf{F_v}$ and $\mathbf{G_v}$ are given by:

$$\mathbf{F_v} = \begin{bmatrix} 0 \\ \tau_{xx} \\ \tau_{xz} \\ u\tau_{xx} + w\tau_{xz} - \dfrac{\mu C_p}{\mathrm{Pr}} \dfrac{\partial T}{\partial x} \end{bmatrix}, \qquad \mathbf{G_v} = \begin{bmatrix} 0 \\ \tau_{xz} \\ \tau_{zz} \\ u\tau_{xz} + w\tau_{zz} - \dfrac{\mu C_p}{\mathrm{Pr}} \dfrac{\partial T}{\partial z} \end{bmatrix}. \tag{9}$$

In Eq. (9) μ is the dynamic viscosity, T is temperature, and Pr is the Prandtl number. The viscous shear stress tensor, τ_{ij} is given by:

$$\begin{bmatrix} \tau_{xx} \\ \tau_{zz} \\ \tau_{xz} \end{bmatrix} = \begin{bmatrix} 2\mu \dfrac{\partial u}{\partial x} - \dfrac{2}{3}\mu \left(\dfrac{\partial u}{\partial x} + \dfrac{\partial w}{\partial z} \right) \\ 2\mu \dfrac{\partial w}{\partial z} - \dfrac{2}{3}\mu \left(\dfrac{\partial u}{\partial x} + \dfrac{\partial w}{\partial z} \right) \\ \mu \left(\dfrac{\partial u}{\partial x} + \dfrac{\partial w}{\partial z} \right) \end{bmatrix}. \tag{10}$$

The viscous terms in the potential temperature based equation set are given by,

$$\mathbf{F_v} = \begin{bmatrix} 0 \\ \mu\rho \dfrac{\partial u}{\partial x} \\ \mu\rho \dfrac{\partial w}{\partial x} \\ \mu\rho \dfrac{\partial \theta}{\partial x} \end{bmatrix}, \qquad \mathbf{G_v} = \begin{bmatrix} 0 \\ \mu\rho \dfrac{\partial u}{\partial z} \\ \mu\rho \dfrac{\partial w}{\partial z} \\ \mu\rho \dfrac{\partial \theta}{\partial z} \end{bmatrix}. \tag{11}$$

Please note that the conservation of energy equation in terms of potential temperature does not take into account the complete viscous stresses. This was first pointed out by Giraldo and Restelli (2008).

III. Numerical Scheme

The Euler equations (2)-(8) in one dimension can be written in the discrete form as:

$$\mathbf{U}_i^{n+1} = \mathbf{U}_i^n - \Delta t\left[\frac{1}{\Delta x}\left(\mathbf{F}_{i+\frac{1}{2}} - \mathbf{F}_{i-\frac{1}{2}}\right)\right], \tag{12}$$

where **U** is the vector of conserved quantities, **F** is the vector of inter-cell fluxes calculated at the control surfaces of each control volume using either an exact or approximate Riemann solver. Δt and Δx are the time step and mesh resolution in *x*-direction respectively. LeVeque (2002) and Bale et al. (2002) suggest using a flux-based wave decomposition, in which the flux differences $\mathbf{F}_i(\mathbf{U}_i) - \mathbf{F}_{i-1}(\mathbf{U}_{i-1})$ are written directly as a linear combination of the right eigenvectors $r_{i-1/2}^p$,

$$\mathbf{F}_i(\mathbf{U}_i) - \mathbf{F}_{i-1}(\mathbf{U}_{i-1}) - \Delta x \psi_{i-1/2} = \sum_{p=1}^{m} \beta_{i-1/2}^p r_{i-1/2}^p \equiv \sum_{p=1}^{m} Z_{i-1/2}^p , \tag{13}$$

and

$$\beta_{i-1/2} = \mathbf{R}_{i-1/2}^{-1}(\mathbf{F}_i(\mathbf{U}_i) - \mathbf{F}_{i-1}(\mathbf{U}_{i-1}) - \Delta x \psi_{i-1/2}) . \tag{14}$$

The vectors $Z^p = \beta^p r^p$ are called *f*-waves and contain flux increments rather than increments in **U**. $\mathbf{R}_{i-1/2}$ is the matrix of right eigenvectors. $\psi = \rho g$, is the source term due to gravity. Eq. (12) can now be re-written as:

$$\mathbf{U}_i^{n+1} = \mathbf{U}_i^n - \frac{\Delta t}{\Delta x}\left[\mathrm{H}^+\Delta\mathbf{U}_{i-1/2} + \mathrm{H}^-\Delta\mathbf{U}_{i+1/2}\right], \tag{15}$$

where

$$\mathrm{H}^-\Delta\mathbf{U}_{i-1/2} = \sum_p Z_{i-1/2}^p \quad if \quad s_{i-1/2}^p < 0 \quad and \quad \mathrm{H}^+\Delta\mathbf{U}_{i-1/2} = \sum_p Z_{i-1/2}^p \quad if \quad s_{i-1/2}^p > 0 . \tag{16}$$

The fluctuations $\mathrm{H}^-\Delta\mathbf{U}_{i-1/2}$ and $\mathrm{H}^+\Delta\mathbf{U}_{i-1/2}$ contribute to the cell-averaged quantity $\mathbf{U}_i$ due to the wave propagation across the cell interfaces. In the above relations, $s_{i-1/2}^p$ are the wave speeds given by the eigenvalues of the hyperbolic equation set. Higher-order accuracy in space can be achieved by adding a correction term (LeVeque 1996: LeVeque 2002):

$$\mathbf{U}_i^{n+1} = \mathbf{U}_i^n - \frac{\Delta t}{\Delta x}\left[\mathrm{H}^+\Delta\mathbf{U}_{i-1/2} + \mathrm{H}^-\Delta\mathbf{U}_{i+1/2}\right] - \frac{\Delta t}{\Delta x}\left[\tilde{\mathbf{F}}_{i+1/2} - \tilde{\mathbf{F}}_{i-1/2}\right], \tag{17}$$

where

$$\tilde{\mathbf{F}}_{i-1/2} = \frac{1}{2}\sum_{p=1}^{m} \mathrm{sgn}(s_{i-1/2}^p)\left[1 - \frac{\Delta t}{\Delta x}\left|s_{i-1/2}^p\right|\right]\tilde{Z}_{i-1/2} , \tag{18}$$

and, $\tilde{Z}^p$ is the limited value of Z^p. Given the *f*-waves and the wave speeds, the flux differences can be computed by summing up the left and right going waves across a cell interface. In the above relations the sweep in *x*-direction is implied. Similar methodology can be used for computations in the *z*-direction with the addition of source term due to gravity. The quantities on cell faces are calculated by taking the average of cell-centered quantities on the either side

of the face. The development of the *f*-waves solver for the atmospheric flows given by Eq. (6)-(8) is described in detail by Ahmad and Lindeman (2007).

IV. Results

In this section, the two equation sets are compared with the help of several benchmark cases used for the validation of Euler and Navier-Stokes equations – (1) Rayleigh-Taylor instability (Almgren et al. 2010); (2) non-hydrostatic inertia-gravity waves (Skamarock and Klemp; Ahmad and Lindeman 2007); (3) descent of a vortex pair in neutral atmosphere; and (4) merger of a co-rotating vortex pair (Brandt and Nomura 2007). The first three cases are solutions of the Euler equations, whereas the fourth case (the vortex pair merger) is a solution of the Navier-Stokes equations. All simulations are for two-dimensional cases.

A. Rayleigh-Taylor Instability

Simulation of the Rayleigh-Taylor instability has been described previously in several publications (Almgren et al. 2010; Liska and Wendroff 2003; Li et al. 1996). The computational domain in this case was defined by $(x,z) \in [0,0.5]\times[0,1]\,m$ with $t \in [0,2.5]\,s$. The mesh had a resolution of $\Delta x = \Delta z = 0.00195m$ (256 x 512 cells). Periodic boundary conditions were used in the lateral, and the top and bottom boundaries were set to solid walls. The initial horizontal and vertical velocities were set to zero. The density was set to $\rho_1 = 1kg/m^3$ in the lower half of the domain and $\rho_2 = 2kg/m^3$ in the upper half of the domain. Pressure was initialized using the hydrostatic equation:

$$p(z) = \begin{cases} p_0 - \rho_1 g z & z < L_z/2 \\ p_0 - \rho_1 g L_z/2 - \rho_2 g(z - L_z/2) & z > L_z/2 \end{cases} \tag{19}$$

where p_0 is the reference pressure and was set to $5Pa$. The acceleration due to gravity, g was set to $1m/s^2$. $L_z = 1m$ is the height of the computational domain. A single-mode perturbation was introduced in density at the interface of heavier and lighter fluids:

$$\rho(x,z) = \rho_1 + \frac{\rho_2 - \rho_1}{2}\left[1 + \tanh\left(\frac{z - \psi(x)}{0.005}\right)\right] \tag{20}$$

where

$$\psi(x) = \frac{L_z}{2} + 0.01\frac{\cos(4\pi x) + \cos(4\pi(L_x - x))}{2} \tag{21}$$

In Eq. (21), $L_x = 0.5m$ is the width of the computational domain. The `tanh` function in Eq. (20) is used to smooth the density profile at the interface (Almgren et al. 2010). The time evolution of the instability computed by the two models is shown in Figure 1. The two simulations are similar with the total energy solution showing a slight loss of symmetry at the tip of the heavier fluid at time = $2.5s$.

B. Non-hydrostatic Inertia-Gravity Waves

The simulation of non-hydrostatic inertia-gravity waves (Skamarock and Klemp 1994; Ahmad and Lindeman 2007) is described in this section. The computational domain was defined by $(x,z) \in [0,300]\times[0,10]\,km$ with $t \in [0,3000]\,s$. The mesh had a resolution of $\Delta x = 1km$ and, $\Delta z = 50m$ (300 x 200 cells). Periodic boundary conditions were used in the lateral and the top and bottom boundaries were set to solid walls. The domain was initialized by a constant Brunt-Väisälä frequency, $N = 10^{-2}s^{-1}$. The waves were excited by introducing a potential temperature perturbation given by:

$$\theta(x,z,0) = \Delta\theta_0 \frac{\sin(\pi z/H)}{1 + (x - x_c)^2/a^2} \tag{22}$$

The amplitude of the initial potential temperature perturbation, $\Delta\theta_0$ was set to 10^{-2}K. The height H of the domain was 10km, and the perturbation half width was a = 5km. The perturbation in potential temperature was initialized at $x_c = L_x/3$, where, L_x is the width of the domain (300km). A uniform horizontal velocity of 20m/s was imposed in the domain and the vertical velocity was set to zero.

Figures 2-3 show the potential temperature perturbation at time = 3000s using the conservation of total energy equation and conservation of potential temperature respectively. No differences were observed between the two models. A comparison of the potential temperature perturbation profile along the domain centerline (z = 5km) for the two equation sets is shown in Figure 4.

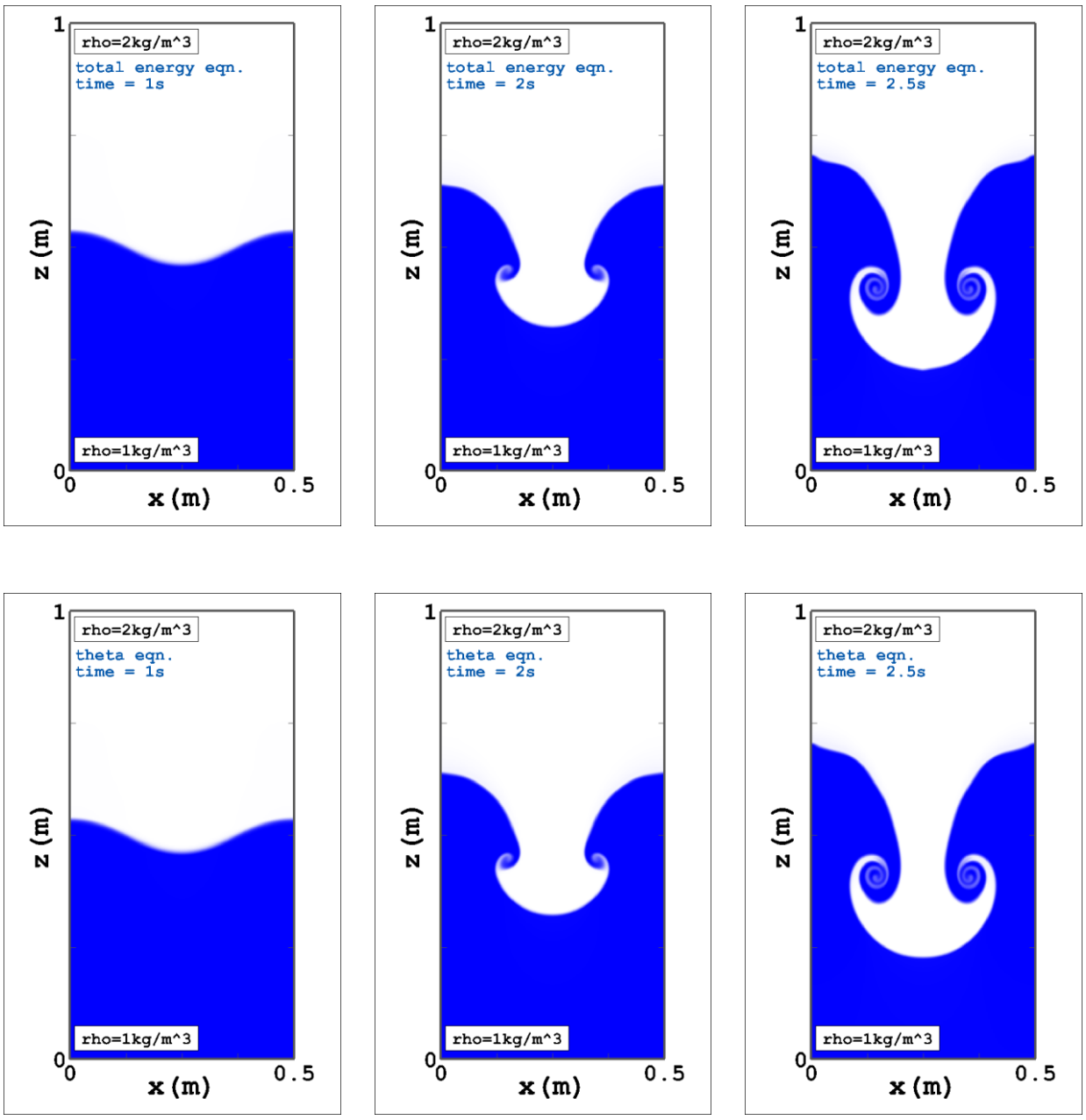

Figure 1. Rayleigh-Taylor Instability. The top row shows the density field at 1s (left), at 2s (middle), and at 2.5s (right) for the total energy equation set and the bottom row shows the density field at 1s (left), at 2s (middle), and at 2.5s (right) for the potential temperature equation set.

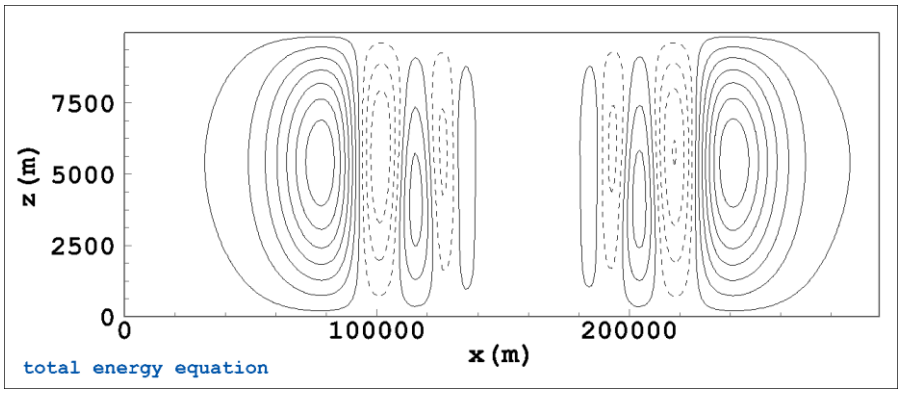

Figure 2. Non-hydrostatic Inertia Gravity Waves. The potential temperature perturbation field (K) at time = 3000*s*. The contours minimum = -0.0014K and the maximum = 0.0025K in the plot. Dashed lines are used for negative values.

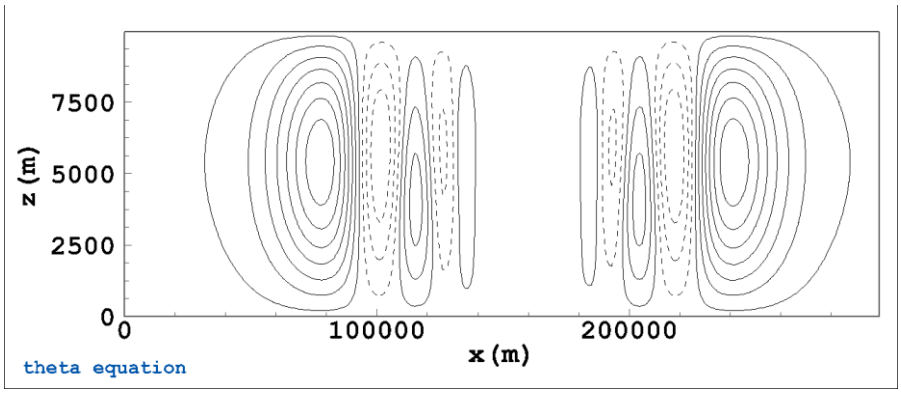

Figure 3. Non-hydrostatic Inertia Gravity Waves. The potential temperature perturbation field (K) at time = 3000*s*. The contours minimum = -0.0014K and the maximum = 0.0025K in the plot. Dashed lines are used for negative values.

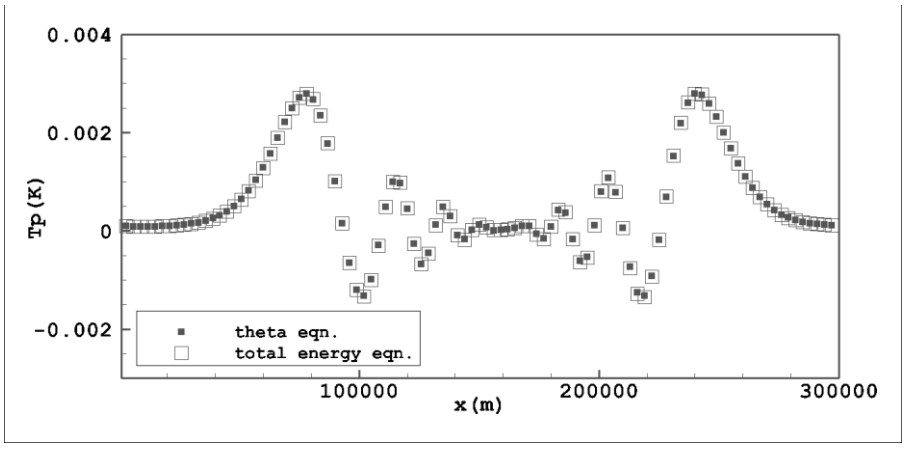

Figure 4. Non-hydrostatic Inertia Gravity Waves. Comparison of potential temperature perturbation (K) values between x = 0 and 300*km*, for z = 5*km* at time = 3000*s*.

C. Vortex Pair Descent in Neutral Atmosphere

Aircraft generate trailing wake vortices as a direct consequence of lift, which merge into a paired system of counter-rotating vortices. The vortex pair descent due to mutual induction and its decay under varying conditions of atmospheric stratification and stability has been a subject of extensive research for several decades (Credeur and Perry 1997; Proctor 1998; Gerz et al. 2002). In this section simulations of vortex pair descent generated by a Boeing 747-400 are described. The computational domain was defined by $(x, z) \in [-300,300] \times [0,600]\, m$ with $t \in [0,120]\, s$. The mesh had a resolution of $\Delta x = \Delta z = 0.6m$ (1000 x 1000 cells). The vortex pair was initialized at $(x_0, z_0) = (0,300)\, m$ using the Burnham-Hallock vortex model (Burnham and Hallock 1982):

$$v_\theta(r) = \frac{\Gamma_0}{2\pi r} \frac{r^2}{r^2 + r_c^2}, \tag{23}$$

where, v_θ is the tangential velocity, $r_c = 4.5m$ is the vortex core radius (v_θ is maximum at $r = r_c$), Γ_0 is the initial vortex circulation ($\Gamma_0 = 565 m^2/s$ for a B747-400 was used in this simulation), and r is the distance from the vortex center (x_0, z_0),

$$r = \sqrt{(x - x_0)^2 + (z - z_0)^2}\ . \tag{24}$$

The tangential velocity in Eq. (23) can be converted to Cartesian velocities using the following relations:

$$\begin{aligned} u(x,z) &= \quad (sign) v_\theta \frac{z}{r} \\ w(x,z) &= -(sign) v_\theta \frac{x}{r} \end{aligned}, \tag{25}$$

where *sign* is used to define the direction of vortex rotation, positive for clockwise and negative for the counter-clockwise direction. The background atmospheric stability was set to zero (the Brunt-Väisälä frequency, $N = 0$). Open/farfield boundary conditions were used in the lateral and at the top. The bottom boundary was set to solid wall.

A comparison of vertical and tangential velocity profiles of the vortex pair at $z = 95.5m$ and time = 120*s*, from the two models is shown in Figure 5. The velocity fields obtained from the two equation sets are almost identical.

Figures 6-8 show the comparison of computed pressure perturbation, and velocity fields obtained from the two models at time = 120*s*. Small differences were observed in the pressure perturbation field with the total energy equation set showing a slightly larger pressure minima.

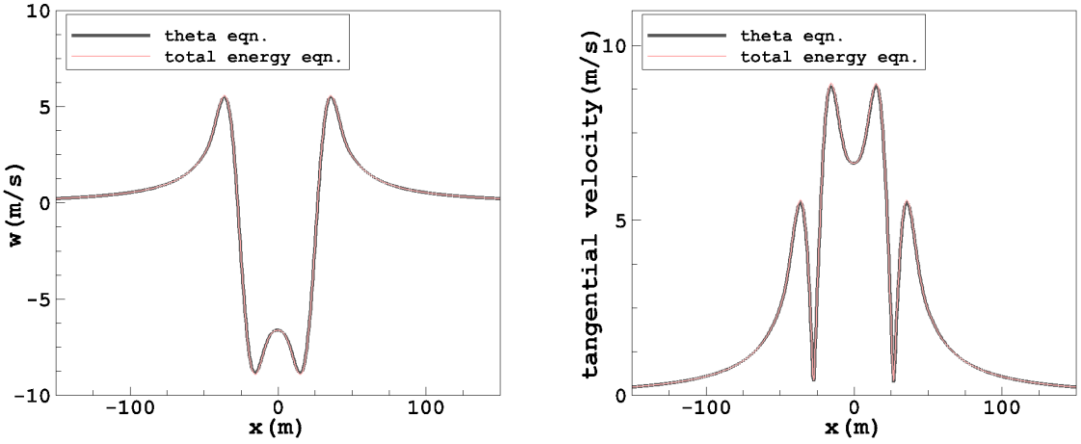

Figure 5. Vortex Pair Descent in Neutral Atmosphere. Comparison of the vertical velocity (*m*/*s*) values between *x* = -150 and 150*m*, for *z* = 95.5*m* at time = 120*s* is shown in the left panel and the tangential velocity (*m*/*s*) is shown in the right panel.

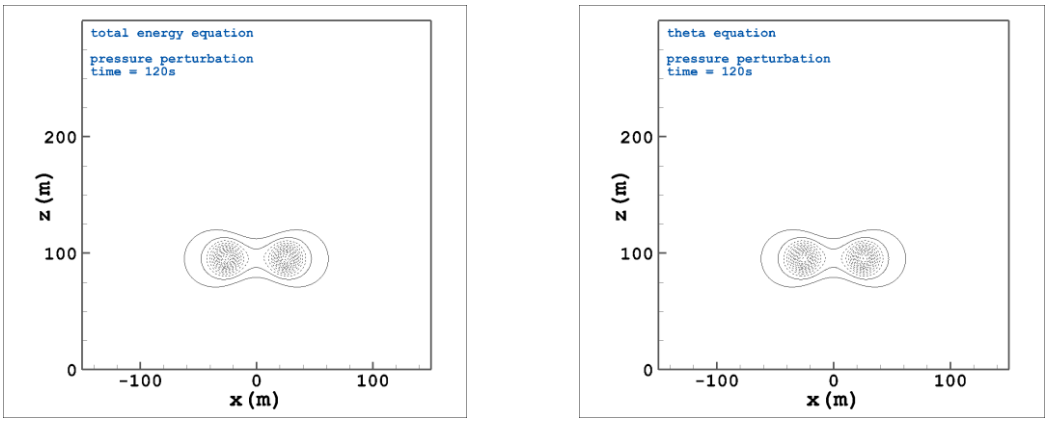

Figure 6. Vortex Pair Descent in Neutral Atmosphere. Pressure perturbation (*Pa*) at time = 120*s*. Solution using total energy conservation equation is shown in the left panel and using potential temperature equation is shown in the right panel. The contours minimum = -72*Pa* and the maximum = 12.5*Pa* in the plot. Dashed lines are used for negative values.

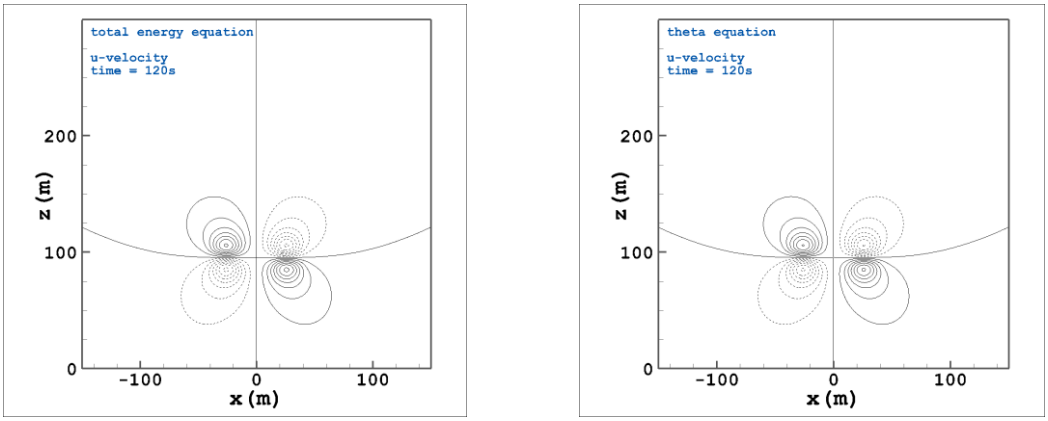

Figure 7. Vortex Pair Descent in Neutral Atmosphere. *u*-velocity (*m*/*s*) at time = 120*s*. Solution using total energy conservation equation is shown in the left panel and using potential temperature equation is shown in the right panel. The contours minimum = -6.3*m*/*s* and the maximum = 6.3*m*/*s* in the plot. Dashed lines are used for negative values.

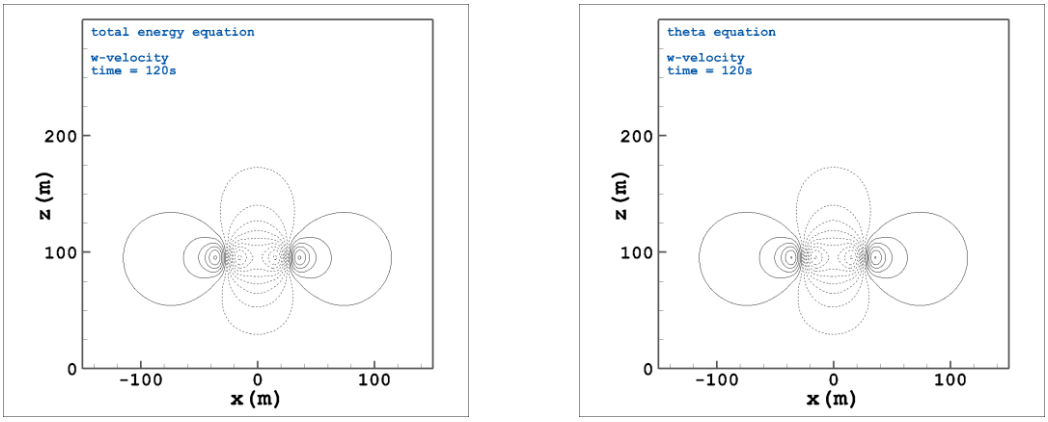

Figure 8. Vortex Pair Descent in Neutral Atmosphere. *w*-velocity (*m*/*s*) at time = 120*s*. Solution using total energy conservation equation is shown in the left panel and using potential temperature equation is shown in the right panel. The contours minimum = -8.8*m*/*s* and the maximum = 5.5*m*/*s* in the plot. Dashed lines are used for negative values.

D. Vortex Merger

The simulation of vortex merger based on Brandt and Nomura (2007) is described in this section. The computational domain was defined by $(x,z) \in [-600,600] \times [0,1200]\, m$ with $t \in [0,124]\, s$. The mesh had a uniform resolution of approximately $1.17m$ in both x and z-directions (1024 x 1024 cells). Farfield/outflow boundary conditions were used for all boundaries. The domain was initialized for a neutral atmosphere by setting the potential temperature at 300K. The vortex pair was initialized at $(x_0, z_0) = (0,600)\, m$ using the Burnham-Hallock vortex model (Burnham and Hallock 1982) with the same rotation direction. Please note that Brandt and Nomura (2007) used a Lamb-Oseen model for their initialization. The vortex pair separation distance was set to $50m$. A circulation Reynolds number, Re_Γ of 5000 was used in the simulation and the Prandtl number was set to 1.

A comparison of the pressure perturbation and tangential velocity at z = 600m and time = 124s, from the two models is shown in Figure 9. At this time both vortices have merged into one vortex. The comparison shows that the results obtained from the two equation sets are identical.

Figures 10-13 show the evolution of vortex merger computed by the two models at different times. At 20s into the simulation the two vortices are rotated by 90 degrees as they move around each other (Figure 10). As the vortices rotate around each other their cores move inwards, eventually merging into a single vortex (Figure 11-13).

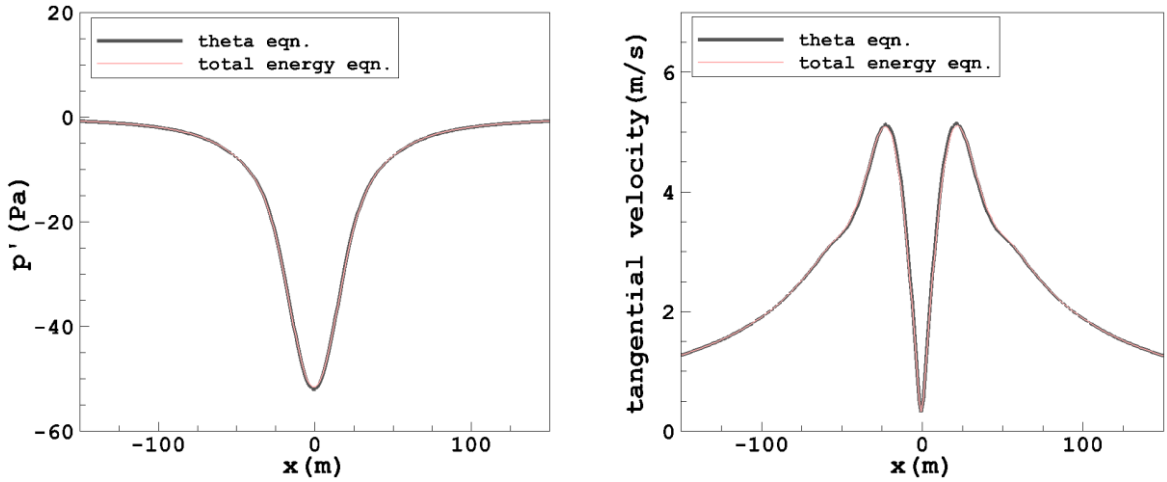

Figure 9. Merger of a Co-rotating Vortex Pair. Comparison of the pressure perturbation (*Pa*) values between x = -150 and 150m, for z = 600m at time = 124s is shown in the left panel and the tangential velocity (m/s) is shown in the right panel.

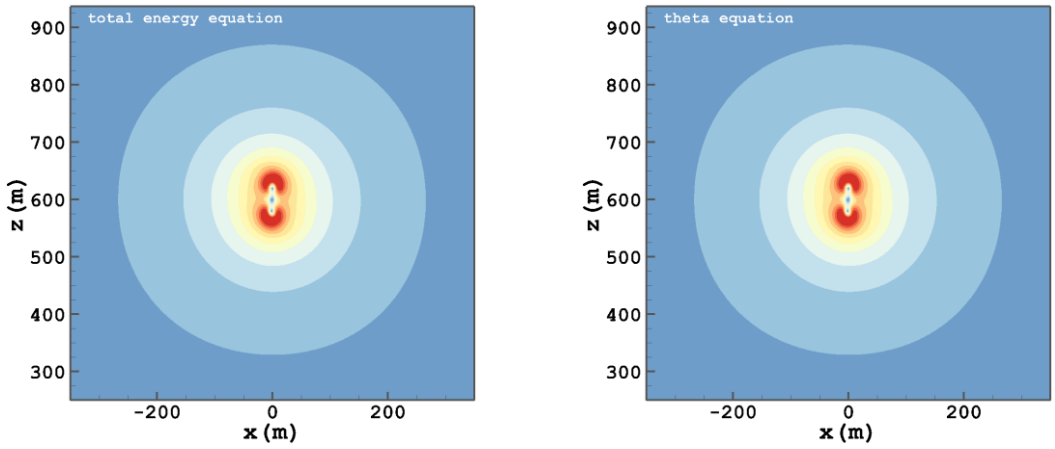

Figure 10. Merger of a Co-rotating Vortex Pair. Tangential velocity (m/s) at time = 20.25s. Solution using total energy conservation equation is shown in the left panel and using potential temperature equation is shown in the right panel. The contours minimum = 0.2m/s and the maximum = 5.25m/s in the plot.

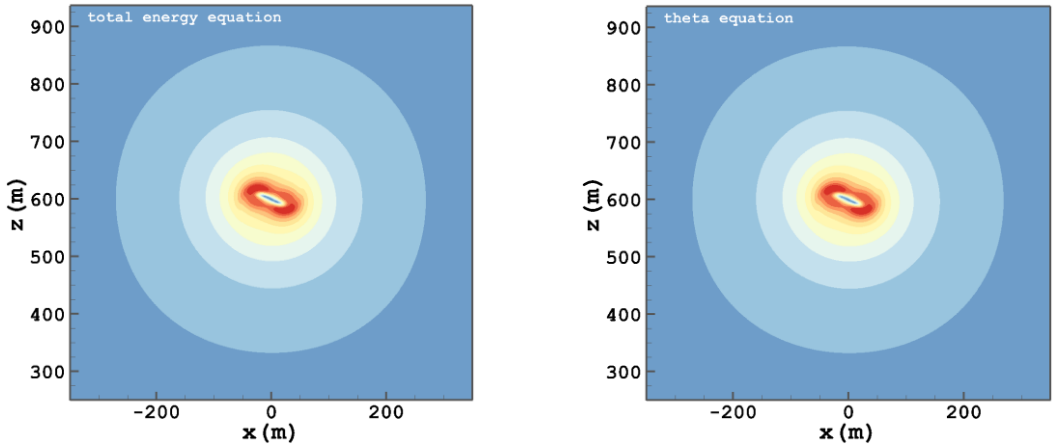

Figure 11. Merger of a Co-rotating Vortex Pair. Tangential velocity (*m/s*) at time = 41.12*s*. Solution using total energy conservation equation is shown in the left panel and using potential temperature equation is shown in the right panel. The contours minimum = 0.2*m/s* and the maximum = 5.25*m/s* in the plot.

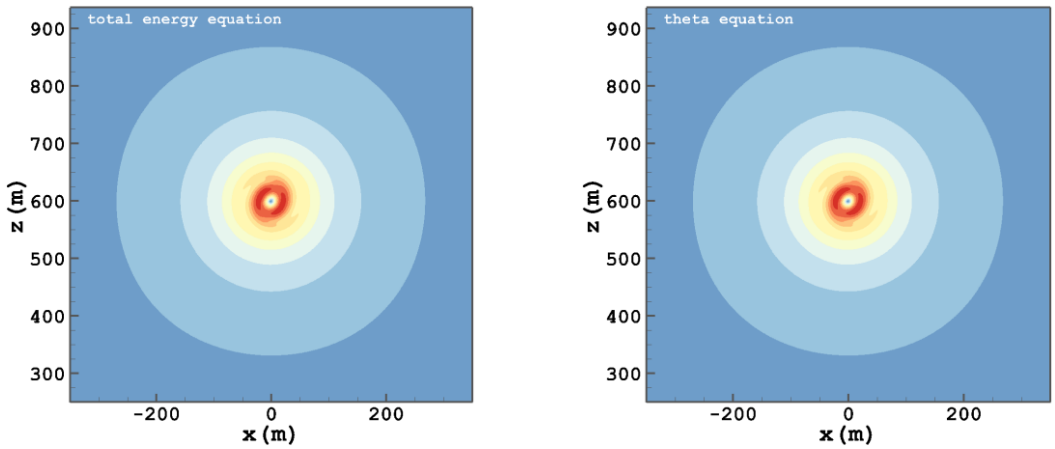

Figure 12. Merger of a Co-rotating Vortex Pair. Tangential velocity (*m/s*) at time = 80.25*s*. Solution using total energy conservation equation is shown in the left panel and using potential temperature equation is shown in the right panel. The contours minimum = 0.2*m/s* and the maximum = 5.25*m/s* in the plot.

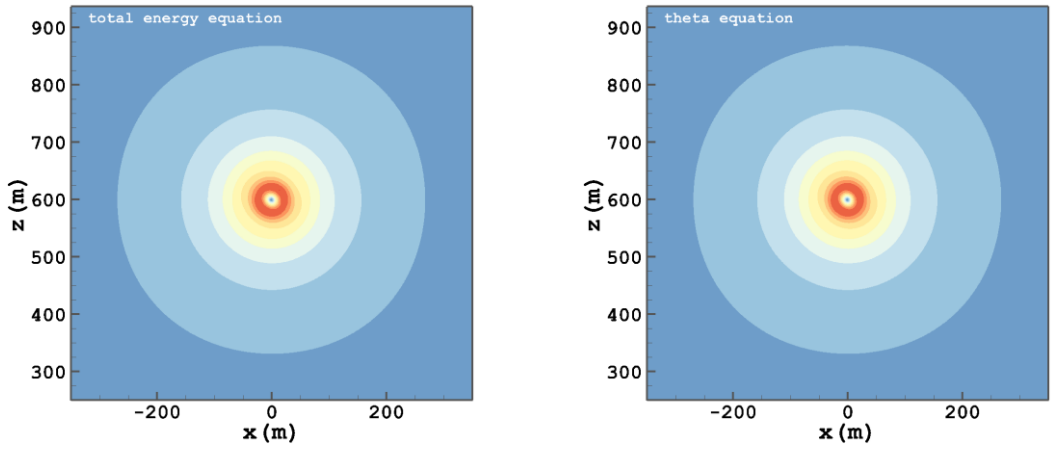

Figure 13. Merger of a Co-rotating Vortex Pair. Tangential velocity (*m/s*) at time = 124*s*. Solution using total energy conservation equation is shown in the left panel and using potential temperature equation is shown in the right panel. The contours minimum = 0.2*m/s* and the maximum = 5.25*m/s* in the plot.

V. Summary

Euler and Navier-Stokes solutions obtained from two different equations sets were compared for atmospheric flow simulations at different temporal and spatial scales using several benchmark cases. Simulations showed that the two equation sets gave similar results for most cases and almost identical results in some cases. The computational cost of the two models was also similar. The primitive variable transformation of potential temperature equation set was derived and found to be identical to the transformation for the total energy conservation equations. This result implies that for smooth solutions the two models should give identical results.

Although the viscous terms are treated differently in the two equation sets, the differences between the two solutions for the vortex merger cases were found to be negligible. Similar results were also obtained by Giraldo and Restelli (2008) for the density current test case. It is suggested that the use of total energy conservation equation set for atmospheric flow applications should be further explored.

Appendix A

One-dimensional homogeneous Euler equations in conservative form are written as:

$$\mathbf{U}_t + \mathbf{F}(\mathbf{U})_x = 0\,, \tag{A.1}$$

where **U** is the vector of conserved quantities and **F**(**U**) is the flux vector:

$$\mathrm{U} = \begin{bmatrix} \rho \\ \rho u \\ E \end{bmatrix}, \qquad \mathrm{F} = \begin{bmatrix} \rho u \\ \rho u^2 + p \\ u(E+p) \end{bmatrix}. \tag{A.2}$$

In the absence of shocks, Eq. (A.1)-(A.2) can be re-written in primitive variable form (Toro 1999) as:

$$\mathbf{W}_t + \mathbf{A}(\mathbf{W})\mathbf{W}_x = 0\,, \tag{A.3}$$

where,

$$\mathbf{W} = \begin{bmatrix} \rho \\ u \\ p \end{bmatrix}, \qquad \mathbf{A}(\mathbf{W}) = \begin{bmatrix} u & \rho & 0 \\ 0 & u & 1/\rho \\ 0 & \rho a^2 & u \end{bmatrix} \tag{A.4}$$

It is shown that the transformation to primitive variables for the Euler equations in terms of potential temperature is identical to Eq. (A.4). One-dimensional homogeneous Euler equations in terms of potential temperature are given by:

$$\mathbf{U} = \begin{bmatrix} \rho \\ \rho u \\ \rho\theta \end{bmatrix}, \qquad \mathbf{F} = \begin{bmatrix} \rho u \\ \rho u^2 + p \\ \rho u \theta \end{bmatrix} \tag{A.5}$$

Re-writing Eq. (A.1) and, Eq. (A.5):

$$\frac{\partial \rho}{\partial t} + \frac{\partial \rho u}{\partial x} = 0 \tag{A.6}$$

$$\frac{\partial \rho u}{\partial t} + \frac{\partial \rho u^2}{\partial x} + \frac{\partial p}{\partial x} = 0 \tag{A.7}$$

$$\frac{\partial \rho\theta}{\partial t} + \frac{\partial \rho u\theta}{\partial x} = 0 \tag{A.8}$$

Expanding Eq. (A.6):

$$\frac{\partial \rho}{\partial t} + u\frac{\partial \rho}{\partial x} + \rho\frac{\partial u}{\partial x} = 0 \tag{**A.9**}$$

Expanding Eq. (A.7):

$$u\frac{\partial \rho}{\partial t} + \rho\frac{\partial u}{\partial t} + u^2\frac{\partial \rho}{\partial x} + 2\rho u\frac{\partial u}{\partial x} + \frac{\partial p}{\partial x} = 0 \tag{A.10}$$

Re-write, $2\rho u\frac{\partial u}{\partial x} = \rho u\frac{\partial u}{\partial x} + \rho u\frac{\partial u}{\partial x}$ in Eq. (A.10):

$$u\frac{\partial \rho}{\partial t} + \rho\frac{\partial u}{\partial t} + u^2\frac{\partial \rho}{\partial x} + \rho u\frac{\partial u}{\partial x} + \rho u\frac{\partial u}{\partial x} + \frac{\partial p}{\partial x} = 0 \tag{A.11}$$

Re-arranging the terms in Eq. (A.11):

$$u\left(\frac{\partial \rho}{\partial t} + u\frac{\partial \rho}{\partial x} + \rho\frac{\partial u}{\partial x}\right) + \rho\frac{\partial u}{\partial t} + \rho u\frac{\partial u}{\partial x} + \frac{\partial p}{\partial x} = 0 \tag{A.12}$$

From Eq. (A.9), $\frac{\partial \rho}{\partial t} + u\frac{\partial \rho}{\partial x} + \rho\frac{\partial u}{\partial x} = 0$, therefore,

$$\rho\frac{\partial u}{\partial t} + \rho u\frac{\partial u}{\partial x} + \frac{\partial p}{\partial x} = 0 \tag{A.13}$$

Divide by ρ,

$$\frac{\partial u}{\partial t} + u\frac{\partial u}{\partial x} + \frac{1}{\rho}\frac{\partial p}{\partial x} = 0 \tag{**A.14**}$$

Let, $\rho\theta = C_1 p^{\frac{1}{\gamma}}$, where, $C_1 = \frac{p_0^{1-\frac{1}{\gamma}}}{R_d}$, then Eq. (A.8) can be written as:

$$\frac{\partial C_1 p^{\frac{1}{\gamma}}}{\partial t} + \frac{\partial C_1 p^{\frac{1}{\gamma}} u}{\partial x} = 0 \tag{A.15}$$

C_1 cancels out in Eq. (A.15):

$$\frac{\partial p^{\frac{1}{\gamma}}}{\partial t} + \frac{\partial p^{\frac{1}{\gamma}} u}{\partial x} = 0 \tag{A.16}$$

Expand Eq. (A.16):

$$\frac{1}{\gamma} p^{\frac{1}{\gamma}-1} \frac{\partial p}{\partial t} + p^{\frac{1}{\gamma}} \frac{\partial u}{\partial x} + \frac{1}{\gamma} p^{\frac{1}{\gamma}-1} u \frac{\partial p}{\partial x} = 0 \tag{A.17}$$

Simplify Eq. (A.17),

$$\frac{1}{\gamma} \frac{p^{\frac{1}{\gamma}}}{p} \frac{\partial p}{\partial t} + p^{\frac{1}{\gamma}} \frac{\partial u}{\partial x} + \frac{1}{\gamma} \frac{p^{\frac{1}{\gamma}}}{p} u \frac{\partial p}{\partial x} = 0 \tag{A.18}$$

$p^{\frac{1}{\gamma}}$ cancels out in Eq. (A.18),

$$\frac{1}{\gamma p} \frac{\partial p}{\partial t} + \frac{\partial u}{\partial x} + \frac{u}{\gamma p} \frac{\partial p}{\partial x} = 0 \tag{A.19}$$

Multiply Eq. (A.19) by ρ,

$$\frac{\rho}{\gamma p} \frac{\partial p}{\partial t} + \rho \frac{\partial u}{\partial x} + \frac{\rho u}{\gamma p} \frac{\partial p}{\partial x} = 0 \tag{A.20}$$

Substituting, $a^2 = \frac{\gamma p}{\rho}$,

$$\frac{1}{a^2} \frac{\partial p}{\partial t} + \rho \frac{\partial u}{\partial x} + \frac{u}{a^2} \frac{\partial p}{\partial x} = 0 \tag{A.21}$$

Multiplying Eq. (A.21) by a^2, for the transformation, $\rho\theta \rightarrow p$:

$$\frac{\partial p}{\partial t} + \rho a^2 \frac{\partial u}{\partial x} + u \frac{\partial p}{\partial x} = 0 \tag{**A.22**}$$

The transformation to non-conservative primitive variables is identical to the one obtained for equation set with conservation of energy in terms of total energy in Eq. (A.4):

$$\mathbf{W} = \begin{bmatrix} \rho \\ u \\ p \end{bmatrix}, \qquad \mathbf{A}(\mathbf{W}) = \begin{bmatrix} u & \rho & 0 \\ 0 & u & 1/\rho \\ 0 & \rho a^2 & u \end{bmatrix} \tag{A.23}$$

References

Ahmad, NN, Z Boybeyi, R Löhner, A Sarma, "A Godunov-type Finite-Volume Scheme for Flows on the Meso- and Micro-scales", American Institute of Aeronautics and Astronautics, AIAA Paper 2005-1234.

Ahmad, NN, DP Bacon, A Sarma, D Koračin, R Vellore, Z Boybeyi, and J Lindeman, "Simulations of Non-hydrostatic Atmosphere using Conservation Laws Package", American Institute of Aeronautics and Astronautics, AIAA Paper 2007-84.

Ahmad, NN, and J Lindeman, "Euler Solutions using Flux-based Wave Decomposition". *International Journal for Numerical Methods in Fluids*, Vol. 54:1, 2007, pp. 41-72.

Ahmad, NN, "The *f-wave* Riemann Solver for Meso- and Micro-scale Flows", American Institute of Aeronautics and Astronautics, AIAA Paper 2008-465.

Ahmad, NN, "An Inter-comparison of Two Mathematical Models for Meso- and Micro-scale Atmospheric Dynamics", American Institute of Aeronautics and Astronautics, AIAA Paper 2009-556.

Bacon, DP, NN Ahmad, Z Boybeyi, TJ Dunn, MS Hall, PCS Lee, RA Sarma, MD Turner, K Waight, S Young, and J Zack, "A Dynamically Adapting Weather and Dispersion Model: The Operational Multiscale Environment Model with Grid Adaptivity (OMEGA)", *Monthly Weather Review*, Vol. 128, 2000, pp. 2044-2076.

Baldauf, M, A Seifert, J Förstner, D Majewski, M Raschendorfer, T Reinhardt, "Operational Convective-Scale Numerical Weather Prediction with the COSMO Model: Description and Sensitivities", *Monthly Weather Review*, Vol. 139, 2011, pp. 3887-3905.

Bale, D, RJ LeVeque, S Mitran, and JA Rossmanith, "A wave-propagation method for conservation laws and balance laws with spatially varying flux functions", *SIAM Journal of Scientific Computing*, Vol. 26, 1908, pp. 177-183.

Bauer, LA, "The Relation between Potential Temperature and Entropy", *Physical Review (Series 1)*, Vol. 26, 1908, pp. 177-183.

Brandt, LK, KK Nomura, "The physics of vortex merger and the effects of ambient stable stratification", *Journal of Fluid Mechanics*, Vol. 592, 2007, pp. 413-446.

Burnham, DC, JN Hallock, "Chicago Monostatic Acoustic Vortex Sensing System", U.S. Department of Transportation, DOT-TSC-FAA-79-103, 1982, 206 pp.

Credeur, L, and RB Perry, "Proceedings of the NASA First Wake Vortex Dynamic Spacing Workshop", National Aeronautics and Space Administration, 1997, NASA/CP-97-206235.

Dudhia, J., "A nonhydrostatic version of the Penn State/NCAR mesoscale model: Validation tests and simulation of an Atlantic cyclone and cold front", *Monthly Weather Review*, Vol. 121, 1993, pp. 1493-1513.

Gerz, T, F Holzäpfel, D Darracq, "Commercial aircraft wake vortices," *Progress in Aerospace Sciences*, Vol. 38, 2002, pp. 181-208.

Giraldo, FX, and M Restelli, "A study of spectral element and discontinuous Galerkin methods for the Navier-Stokes equations in nonhydrostatic mesoscale atmospheric modeling: Equations sets and test cases", *Journal of Computational Physics*, Vol. 227, 2008, pp. 3849-3877.

Hodur, RM, "The Naval Research Laboratory's Couples Ocean/Atmosphere Mesoscale Prediction System (COAMPS)", *Monthly Weather Review*, Vol. 125, 1997, pp. 1414-1430.

Klassen, L, D Kroner, and Ph Schott, "Finite volume method on unstructured grids in 3D with applications to the simulation of gravity waves", *Meteorology and Atmospheric Physics*, Vol. 82, 2003, pp. 259-270.

Klemp, JB, WC Skamarock, and J Dudhia, "Conservative Split-Explicit Time Integration Methods for the Compressible Nonhydrostatic Equations," *Monthly Weather Review*, Vol. 135, 2007, pp. 2897-2913.

LeVeque, RJ, "High-resolution conservative algorithms for advection in incompressible flow", *SIAM Journal of Numerical Analysis*, Vol. 33, 1996, pp. 627-665.

LeVeque, RJ, "Finite Volume Methods for Hyperbolic Problems", Cambridge University Press, 2002.

Lilly, DK, "On the Numerical Simulation of Buoyant Convection", *Tellus*. Vol. 14, 1962, pp. 148-172.

Pielke, R, WR Cotton, RL Walko, CJ Tremback, WA Lyons, LD Grasso, ME Nicholls, "A Comprehensive Meteorological Modeling System – RAMS", *Meteorology and Atmospheric Physics*, Vol. 49, 1992, pp. 69-91.

Proctor, FH, "The NASA Langley Wake Vortex Modeling Effort in Support of an Operational Aircraft Spacing System", American Institute of Aeronautics and Astronautics, AIAA Paper 1998-0589.

Skamarock, WC, and JB Klemp, "Efficiency and Accuracy of the Klemp-Wilhelmson Time-Splitting Technique", *Monthly Weather Review*, Vol. 122, 1994, pp. 2623-2630.

Snively, JB, and VP Pasko, "Breaking of thunderstorm-generated gravity waves as a source of short-period ducted waves at mesopause altitudes", *Geophysical Research Letters*, Vol. 30, 2003, pp. 2254-2258.

Straka, JM, RB Wilhelmson, LJ Wicker, JR Anderson, and KK Droegemeier, "Numerical Solutions of a Non-linear Density Current: A Benchmark Solution and Comparisons", *International Journal for Numerical Methods in Fluids*, Vol. 17, 1993, pp. 1-22.

Toro, E. F., **"**Riemann Solvers and Numerical Methods for Fluid Dynamics", Springer-Verlag, 1999.

Xue, M, KK Droegemeier, and V Wong, "The Advanced Regional Prediction System (ARPS) – A multi-scale nonhydrostatic atmospheric simulation and prediction model. Part I: Model dynamics and verification", *Meteorology and Atmospheric Physics*, Vol. 75, 2000, pp. 161-193.